Title

Osmotic Energy Conversion in Deep-Sea Hydrothermal Vents

Hye-Eun Lee[1]*, Tomoyo Okumura[2], Hideshi Ooka[1], Kiyohiro Adachi[3], Takaaki Hikima[4], Kunio Hirata[4], Yoshiaki Kawano[4], Hiroaki Matsuura[4], Masaki Yamamoto[4], Masahiro Yamamoto[5], Akira Yamaguchi[1,6], Ji-Eun Lee[1], Ki Tae Nam[7], Yasuhiko Ohara[5,8,9], Daisuke Hashizume[3], Shawn Erin McGlynn[1,10], Ryuhei Nakamura[1,10]*

1 RIKEN Center for Sustainable Resource Science, Wako, Saitama, Japan

2 Kochi University, Nankoku, Kochi, Japan

3 RIKEN Center for Emergent Matter Science, Wako, Saitama, Japan

4 RIKEN SPring-8 Center, Hyogo, Japan

5 Japan Agency for Marine-Earth Science and Technology, Yokosuka, Kanagawa, Japan

6 Department of Materials Science and Engineering, Tokyo Institute of Technology, Tokyo, Japan

7 Department of Materials Science and Engineering, Seoul National University, Seoul, South Korea

8 Hydrographic and Oceanographic Department of Japan, Tokyo, Japan

9 Graduate School of Environmental Studies, Nagoya University, Nagoya, Japan

10 Earth-Life Science Institute, Tokyo Institute of Technology, Tokyo, Japan

*Corresponding authors

Correspondence to Hye-Eun Lee or Ryuhei Nakamura

Abstract

Selective ion transport through nanochannels plays a crucial role in osmotic energy conversion in cellular systems. We show that this cell-essential process occurs in a submarine hydrothermal vent (HV) precipitate derived from a serpentine-hosted geological environment. Plate-like layered nanocrystals are aligned on the nano to millimeter scale, forming confined nanochannels in the HV precipitate. The nanochannels with surface charges function as a cation- and anion-selective ion transport membrane, allowing the precipitates to convert ionic gradients of Na^+, K^+, H^+, and Cl^- into electrical energy. Our findings suggest that osmotic energy conversion can occur spontaneously and widely through geological processes, offering valuable insights into the establishment of electrochemically coupled ion transport in early life as well as the creation of self-organized structures in engineering fields.

Main Text

Gradients such as temperature, pressure, redox and concentration are ubiquitous in nature. Converting these gradients into usable energy would make them accessible as continuous energy sources. In nature, cells interconvert electrochemical, ion, and chemical gradients using respiratory protein complexes embedded in a membrane[1,2]. Ionic gradients are recently also being harnessed as energy sources in material science using 2D materials and nanostructures[3-9].

Submarine HVs are fascinating geological systems surrounded by steep, long-lasting gradients and have long been hypothesized to function as naturally derived energy converters, leading to the formation of the first cells[10-21]. HVs form when the hot, ion-rich vent fluid solution are injected into the cold, oxidizing seawater leading to precipitation, and can form from a diverse range of geologic activity[22] – for example along mid-ocean ridges[23,24] (on-axis) and away from spreading centers[25,26] (off-axis). Off-axis HVs mainly form by the hydrolysis of olivine ($(Mg,Fe)_2SiO_4$), which generates alkaline fluids with diverse ions[16,27,28]. Subsequent mixing with ocean water generates porous, interconnected precipitates rich in oxides and carbonates which forms microscale inorganic walls which function as a diffusion barrier, maintaining steep chemical gradients in the two solutions[26]. Here we provide the first detailed structural insight into HV precipitates formed by the hydrolysis of olivine. The HV wall contains nanopores, aligned structures and variable surface charges, leading to osmotic energy conversion through diverse ionic gradients present in the submarine environment. Osmotic energy conversion in HVs, similar to those found in cellular mechanisms, may suggest an evolutionary relevance between HVs and cells.

Structure of HVs with nanopores

The HV precipitates examined here (Fig. 1a) were collected from the Shinkai Seep Field (SSF), which is located in the southern Mariana Trench, Pacific Ocean at a depth of 5743 m (11°39.38′N, 143°2.73′E)[29]. The geochemistry in the SSF is primarily related to serpentinization, a process that forms serpentine from olivine. During the initial stages of HV formation in the SSF, a brucite-rich white chimney forms and the mineral composition of the HV precipitates change from predominantly brucite to carbonate-rich as the discharge fluid activity reduced[29]. Cross-polarized optical microscopy (POM; Fig. 1b, c) revealed a complex internal structure comprised of porous columnar structures that served as channels for

discharging the vent fluid. The fluid channels were separated by 200 ~ 400-μm thick inorganic walls that were mainly composed of brucite, a layered hydroxide crystal, (Fig. 1c, SI Fig. 1, 2) and exhibited a periodic lamellar structure with a wall thickness of ~ 10 μm (Fig. 1c (red arrows), d, e). The sublayers of this structure consisted of consolidated plate-like brucite nanocrystals with a diameter of ~ 100 nm that were perpendicularly aligned to the surface of channel (Fig. 1f, g, h). In an enlarged high-angle annular dark-field scanning transmission electron microscopy (HAADF-STEM) image (Fig. 1i), individual crystals contained porous nanostructures (2 ~ 3 nm) that appeared as local density variations. Nitrogen adsorption-desorption isotherm analysis identified slit-like nanopores in the inorganic walls with a various pore size ranging from 2 to 100 nm that originated from the multiple hierarchical stacking of plate-like structures (SI Fig. 3).

Alignment of brucite across the macro scale

The alignment of the brucite nanocrystals within the HV precipitates was further analyzed using synchrotron radiation X-ray diffraction (wide-angle X-ray scattering (WAXS)) scanning. Multiple areas of the horizontal slice of HV samples were scanned using a 5-μm X-ray beam and a scattering intensity map was constructed from the total intensity of the diffractograms (Fig. 2a). Similar to that seen in the POM and SEM images, a band-like structure was observed, due to the periodic density changes of the brucite crystals within the HV wall (Fig. 2a, SI Fig. 4a, b). Pronounced anisotropy of brucite 001 diffraction was detected, indicating that (001) plane of brucite orients preferentially along the [001] crystallographic direction (Fig. 2b, c, SI Fig. 4c, d). The directionality of preferential orientation of brucite (001) planes was varied depending on the locations (Fig. 2b, c) and a schematic of the layered (001) plane of brucite with corresponding *c*-axis was shown below each WAXS pattern (Fig. 2c, bottom).

We next extracted the diffraction intensities of the anisotropic rings and azimuthal angles of the highest intensity in the WAXS data and created a two-dimensional vector field map, with the vector directions indicating the preferred orientation direction of the (001) plane along the [001] direction or *c*-axis, and the vector colors and lengths representing the relative amount of plane alignment (Fig. 2d, e). For example, the ring patterns of 3 and 4 (Fig. 2 c) are represented by a red vector in the top right and a green vector in the bottom right, respectively. Notably, over the entire scanned area, the vector plot shows a continuous change in the direction of preferred orientation, suggesting that the brucite layers are arranged in a concentric manner radiating outwards from the fluid channel (Fig 2e, f). The alignment of brucite nanocrystals

along the channel continues throughout the entire sample even when the wall structure bends, diverges, or converges (Fig. 2e, SI Fig. 5a, b). The crystal alignment was also observed in the vertical HV slices (SI Fig. 6, Supplementary Notes). WAXS mapping using a larger, 100-μm X-ray beam size further confirmed that the continuous alignment of the nanocrystals in the walls extended to millimeter-scale (2.5 × 6.0 mm; SI Fig. 5c, d). Long-range alignment of the brucite nanocrystals was corroborated by POM analysis conducted with a retardation plate (first order, 530 nm; SI Fig. 5e). The yellow and blue interference colors alternating along the angular direction of the inorganic wall represent the radial configuration of crystals surrounding the channel and are consistent with the schematic illustration presented in Fig. 2f.

The periodic banding pattern and crystal arrangements found in the HV samples are features that frequently appear in a system, in which chemical (reaction) and physical (diffusion) processes are combined[30-32]. Reactions involving transport phenomena such as diffusion or flow intrinsically provide spatially varying concentrations which may lead to the formation of complex self-organized patterns[33-35]. Especially in systems with an internal feedback, such as precipitation accompanied by a pH change, ionic concentrations can show spatial and temporal oscillation, resulting in periodic patterns in the structure[36,37]. The formation of HVs generated by the injection of alkaline fluids is a flow-driven formation system, and there are also periodic fluctuations in the flow around the HVs[38]. The repetitive banded texture in the HV samples (Figs. 1, 2) and the periodic formation of areas rich in OH bonds within brucite crystals (SI Fig. 7) suggest a reaction-diffusion mechanism in HV formation. The crystal arrangement observed in the HV samples may be attributable to diffusiophoresis, a phenomenon in which charged particles move along a concentration gradient of ions, such as NaCl, KCl, protons, and hydroxides[39-41]. During HV formation, a concentration gradient is established between charged brucite precipitates in the vent fluid and seawater[42-44]. The resulting diffusiophoretic field would provide a directional driving force to the charged precipitates and may promote the concentric arrangement of particles around the channels (Supplementary Notes).

Ion adsorption and surface charge of HV minerals

In addition to flow-driven hierarchical structures in HV mineral, the pores show variable surface charges depending on adsorbed ions. Brucite crystals rich in carbonate ions were detected at several locations in the inorganic HV wall (Fig. 3b, red spectrum; Fig. 3c, blue Raman map). Additionally, crystals with different refractive indices were also observed on the surface at these locations (Fig. 3d) and were identified by Raman and X-ray diffraction

mapping as Mg-carbonate crystals (Fig. 3a-c, Supplementary Notes). The existence of both brucite with carbonate ions and Mg-carbonate crystals indicates that the interconnected HV channels are exposed to various inorganic ions that are present in the hydrothermal fluid and seawater. As brucite is able to adsorb a wide variety of inorganic ions[45,46], the surface charge of HV precipitates can significantly change depending on the composition of the surrounding fluids (Fig. 3e, f). Indeed, Raman analysis of natural HV samples confirmed that brucite, which is the main constituent mineral of HVs, adsorbs K^+, Ca^{2+}, CO_3^{2-}, NO_3^-, and SO_4^{2-} (Fig. 3e). Furthermore, the zeta potential of the HV samples varied greatly depending on the type of adsorbed ion, from - 30 mV (CO_3^{2-}) to + 25 mV (Ca^{2+}), indicating that the electrostatic properties of the HV surface are markedly influenced by the interaction with inorganic ions present in the environment (Fig. 3f).

Osmotic energy conversion in HVs

Nanopores, structural alignment, and variable surface charges found in HVs are hallmarks of materials associated with osmotic energy conversion[3-9]. Materials with high surface charge density and confined nanopores have been designed and used for industrial power generation systems from salinity gradients between seawater and river water[3-5]. Motivated by the findings above, we tested the osmotic energy conversion in the HV.

The HV samples were exposed to various concentrations of KCl and the current response was plotted (Fig. 4a). At high KCl concentrations ranging from 1 M to 1 mM, the conductance of HVs is proportional with the salt concentration, indicating that electrolyte properties dictate ionic conductivity. However, the conductance remained constant even when the KCl concentration was decreased below 1 mM KCl, which is a significant deviation from the bulk characteristic of ion transport seen at higher concentrations. This plateau in the conductance is indicative of surface charge-governed ion transport[47] and suggests that this process dominates ion transport in HV nanopores.

The HV samples were next exposed to geologically plausible chemical gradient conditions by placing them at the interface of two KCl solutions (0.1 mM and 0.1 M). A two-chamber electrochemical cell equipped with an Ag/AgCl electrode (SI Fig. 8a, b) was used to record the current-voltage (*I-V*) response of the HV samples that had been adsorbed with either CO_3^{2-} or Ca^{2+} (Fig. 4b, $N = 15$, SI Fig. 8c-e). When carbonate ions were adsorbed to the HV nanopore walls, a negative surface charge was generated (Supplementary Notes). Further, when the HV

nanopores were exposed to KCl, electrical double layers (EDLs) were created within the nanopores depending on the KCl concentration (Debye screening length = 0.96 and 30.42 nm for 0.1 M and 0.1 mM KCl, respectively). In the HV mineral wall, the dominant pore size is 60 nm (SI Fig. 3b), indicating that a 30 nm EDL formed by 0.1 mM KCl is completely overlapped inside the HV nanopore. The overlap of EDL within the narrow nanopores effectively results in a screen barrier permeable only to ions with a specific charge. This allows selective ion transport, a mechanism known as surface charge-governed ion transport. Furthermore, the continuous arrangement of crystalline, together with the slit-like pores (Figs. 1, 2, SI Fig. 3), suggests that the HV inorganic walls can act as large membranes that can provide ion transport channels. The selectively transported ions can then be exploited for redox reactions at the electrode, resulting in electrochemical power generation.

In the presence of a KCl gradient, the open circuit voltage (V_{oc}) of the CO_3^{2-} ion adsorbed sample was determined to be 229 mV (SI Fig. 8c, blue circle). Subtracting the redox potential of the Ag/AgCl electrode (V_{redox}, 163 mV; Method, SI Table) yielded a pure osmotic potential (V_{os}, diffusion potential) of 66 mV for the HV sample shown in Fig. 4b (blue circle). In contrast, a negative V_{os} value of - 46 mV was observed when Ca^{2+} ions were adsorbed (Fig. 4b, red circle). This change in the V_{os} indicates that the surface charge resulting from CO_3^{2-} and Ca^{2+} adsorption plays a key role for the selective transport of cations and anions in HV nanopores. Namely, the change of V_{os} indicates that the dominant charge carrier is shifted from K^+ to Cl^- upon switching the adsorbed ions from CO_3^{2-} to Ca^{2+}. The V_{os} and diffusion current (I_{os}) increased proportionally with the ionic concentration difference (SI Fig. 9a, b), confirming that the detected electrical energy originates from the chemical potential gradient. Furthermore, due to the cation- and anion-selective nature of HV walls, connecting positively and negatively charged HV sample pairs in series increased diffusion potentials, demonstrating that this configuration allows the HV precipitates to harness the chemical potential gradient more effectively (SI Fig. 9c). When the direction of the HV sample was rotated 90° from the natural HV configuration, I_{os} was lower than that of the HV's natural direction, suggesting that the arrangement of brucite in HV precipitates facilitates selective ion transport (Supplementary Notes).

Selective ion transport within HV precipitates was further examined by the direct measurement of Na^+ and Cl^- ions over time (Fig. 4c, d, SI Fig. 9d). Cation- (CO_3^{2-}-adsorbed) and anion-selective (Ca^{2+}-adsorbed HV) HV samples were fixed between two reservoirs filled with either

low (0.1 mM) or high (0.1 M) salt concentrations and the concentration changes of the Na^+ and Cl^- ions were monitored with respect to time (Fig. 4c). In the case of Na^+ ion transport through CO_3^{2-}-adsorbed HV nanopores, the concentration of Na^+ ions in the low concentration reservoir gradually increased over time. In contrast, there was minimal change in the Na^+ ion concentration across the Ca^{2+}-adsorbed HV sample (Fig. 4d). Instead, the Cl^- increased steadily on this side of the reactor, indicating that HV precipitates are capable of selective ion transfer.

One of the most characteristic features of serpentinite-hosted HV systems is the presence of a large pH gradient between the seawater (pH ~ 7) and vented fluids (pH ~ 9-11). To examine conversion of a pH gradient to electrochemical energy, the cation-selective (CO_3^{2-}-adsorbed) HV sample was placed between reservoirs containing pH 10 and 4 solutions and the electrical response was measured (Fig. 4e, gray circle). Under these conditions, 55 mV of V_{os} and -2 nA of I_{os} were generated. The cation-selective HV sample was also subjected to a deuterium gradient (pD) and the *I-V* response was monitored (Fig. 4e, red circle). The I_{os} decreased by 2.3 fold compared to pH gradient case, while the potential was similar, indicating that proton movement was the source of the generated current. In contrast, when the anion-selective HV sample was subjected to the same test, a reduced H/D kinetic isotope effect was observed, suggesting that hydroxide is involved in the power generation (SI Fig. 10).

Discussion

The findings from the present study provide experimental evidence for geochemistry-driven organization of the inorganic structure and energy conversion function of serpentine-hosted HV systems. HV research over the last 40 years has profoundly advanced our views of life and Earth[16], and deep-sea HV harbors ecosystems distinct from terrestrial life where microbes are closely interconnected with the HV environment[48]. Due to the enriched redox environment and the similarity of these chemical gradients with those found across cell membranes, HVs have been proposed as the evolutionary starting point for the basic building blocks of primordial life[10-21]. Our study shows that membrane-based energy conversion similar to those observed in modern cells can occur across HV precipitates even in simple geological environments. The discovery of ongoing hydrothermal activities on other icy satellites[49] extends the implications of HV research to life beyond Earth.

Main References

1 Mitchell, P. Coupling of phosphorylation to electron and hydrogen transfer by a chemi-osmotic type of mechanism. *Nature* **191**, 144-148 (1961).

2 Schoepp-Cothenet, B. *et al.* On the universal core of bioenergetics. *Biochim. Biophys. Acta.* **1827**, 79-93 (2013).

3 Xiao, K., Jiang, L. & Antonietti, M. Ion transport in nanofluidic devices for energy harvesting. *Joule* **3**, 2364-2380 (2019).

4 Macha, M., Marion, S., Nandigana, V. V. R. & Radenovic, A. 2D materials as an emerging platform for nanopore-based power generation. *Nat. Rev. Mater.* **4**, 588-605 (2019).

5 Zhang, Z., Wen, L. & Jiang, L. Nanofluidics for osmotic energy conversion. *Nat. Rev. Mater.* **6**, 622-639 (2021).

6 Guo, W. *et al.* Energy harvesting with single-ion-selective nanopores: a concentration-gradient-driven nanofluidic power source. *Adv. Funct. Mater.* **20**, 1339-1344 (2010).

7 Kim, D.-K., Duan, C., Chen, Y.-F. & Majumdar, A. Power generation from concentration gradient by reverse electrodialysis in ion-selective nanochannels. *Microfluid Nanofluid.* **9**, 1215-1224 (2010).

8 Siria, A. *et al.* Giant osmotic energy conversion measured in a single transmembrane boron nitride nanotube. *Nature* **494**, 455-458 (2013).

9 Feng, J. *et al.* Single-layer MoS_2 nanopores as nanopower generators. *Nature* **536**, 197-200 (2016).

10 Baross, J. A. & Hoffman, S. E. Submarine hydrothermal vents and associated gradient environments as sites for the origin and evolution of life. *Orig. Life Evol. Biosph.* **15**, 327-345 (1985).

11 Wächtershäuser, G. Pyrite formation, the first energy source for life: a hypothesis. *Syst. Appl. Microbiol.* **10**, 207-210 (1988).

12 Russell, M. J., Hall, A. J. & Turner, D. In vitro growth of iron sulphide chimneys: possible culture chambers for origin-of-life experiments. *Terra Nova* **1**, 238-241 (1989).

13 Wächtershäuser, G. Groundworks for an evolutionary biochemistry: the iron-sulphur world. *Prog. Biophys. Mol. Biol.* **58**, 85-201 (1992).

14 Russell, M. J. & Hall, A. J. The emergence of life from iron monosulphide bubbles at a submarine hydrothermal redox and pH front. *J. Geol. Soc. London* **154**, 377-402 (1997).

15 Martin, W. & Russell, M. J. On the origins of cells: a hypothesis for the evolutionary transitions from abiotic geochemistry to chemoautotrophic prokaryotes, and from prokaryotes to nucleated cells. *Philos. Trans. R. Soc. Lond., B, Biol. Sci.* **358**, 59-85 (2003).

16 Martin, W., Baross, J., Kelley, D. & Russell, M. J. Hydrothermal vents and the origin of life. *Nat. Rev. Microbiol.* **6**, 805-814 (2008).

17 Lane, N. & Martin, W. F. The origin of membrane bioenergetics. *Cell* **151**, 1406-1416 (2012).

18 Nakamura, R. *et al.* Electrical current generation across a black smoker chimney. *Angew. Chem. Int. Ed. Engl.* **49**, 7692-7694 (2010).

19 Kitadai, N. *et al.* Metals likely promoted protometabolism in early ocean alkaline hydrothermal systems. *Sci. Adv.* **5**, eaav7848 (2019).

20 Hudson, R. *et al.* CO_2 reduction driven by a pH gradient. *Proc. Natl. Acad. Sci. U. S. A.* **117**, 22873-22879 (2020).

21 Preiner, M. *et al.* A hydrogen-dependent geochemical analogue of primordial carbon and energy metabolism. *Nat. Ecol. Evol.* **4**, 534-542 (2020).

22 Tivey, M. Generation of seafloor hydrothermal vent fluids and associated mineral deposits. *Oceanography* **20**, 50-65 (2007).

23 Francheteau, J. *et al.* Massive deep-sea sulphide ore deposits discovered on the East Pacific Rise. *Nature* **277**, 523-528 (1979).

24 Spiess, F. N. *et al.* East pacific rise: hot springs and geophysical experiments. *Science* **207**, 1421-1433 (1980).

25 Kelley, D. S. *et al.* An off-axis hydrothermal vent field near the Mid-Atlantic Ridge at 30 degrees N. *Nature* **412**, 145-149 (2001).

26 Kelley, D. S. *et al.* A serpentinite-hosted ecosystem: the Lost City hydrothermal field. *Science* **307**, 1428-1434 (2005).

27 Sleep, N. H., Meibom, A., Fridriksson, T., Coleman, R. G. & Bird, D. K. H_2-rich fluids from serpentinization: geochemical and biotic implications. *Proc. Natl. Acad. Sci. U. S. A.* **101**, 12818-12823 (2004).

28 Proskurowski, G. *et al.* Abiogenic hydrocarbon production at lost city hydrothermal field. *Science* **319**, 604-607 (2008).

29 Okumura, T. *et al.* Brucite chimney formation and carbonate alteration at the Shinkai Seep Field, a serpentinite-hosted vent system in the southern Mariana forearc. *Geochem. Geophys. Geosyst.* **17**, 3775-3796 (2016).

30 Nakouzi, E. & Steinbock, O. Self-organization in precipitation reactions far from the equilibrium. *Sci. Adv.* **2**, e1601144 (2016).

31 Epstein, I. R. & Xu, B. Reaction-diffusion processes at the nano- and microscales. *Nat. Nanotechnol.* **11**, 312-319 (2016).

32 Barge, L. M. *et al.* From chemical gardens to chemobrionics. *Chem. Rev.* **115**, 8652-8703 (2015).

33 Heaney, P. J. & Davis, A. M. Observation and origin of self-organized textures in agates. *Science* **269**, 1562-1565 (1995).

34 Capito, R. M., Azevedo, H. S., Velichko, Y. S., Mata, A. & Stupp, S. I. Self-assembly of large and small molecules into hierarchically ordered sacs and membranes. *Science* **319**, 1812-1816

(2008).

35 Noorduin, W. L., Grinthal, A., Mahadevan, L. & Aizenberg, J. Rationally designed complex, hierarchical microarchitectures. *Science* **340**, 832-837 (2013).

36 Montalti, M. *et al.* Local pH oscillations witness autocatalytic self-organization of biomorphic nanostructures. *Nat. Commun.* **8**, 14427 (2017).

37 Garcia-Ruiz, J. M., Melero-Garcia, E. & Hyde, S. T. Morphogenesis of self-assembled nanocrystalline materials of barium carbonate and silica. *Science* **323**, 362-365 (2009).

38 Barreyre, T. & Sohn, R. A. Poroelastic response of mid-ocean ridge hydrothermal systems to ocean tidal loading: Implications for shallow permeability structure. *Geophys. Res. Lett.* **43**, 1660-1668 (2016).

39 Abecassis, B., Cottin-Bizonne, C., Ybert, C., Ajdari, A. & Bocquet, L. Boosting migration of large particles by solute contrasts. *Nat. Mater.* **7**, 785-789 (2008).

40 Velegol, D., Garg, A., Guha, R., Kar, A. & Kumar, M. Origins of concentration gradients for diffusiophoresis. *Soft Matter* **12**, 4686-4703 (2016).

41 Shim, S. Diffusiophoresis, diffusioosmosis, and microfluidics: surface-flow-driven phenomena in the presence of flow. *Chem. Rev.* **122**, 6986-7009 (2022).

42 Barge, L. M. *et al.* Characterization of iron-phosphate-silicate chemical garden structures. *Langmuir* **28**, 3714-3721 (2012).

43 Barge, L. M. *et al.* From chemical gardens to fuel cells: generation of electrical potential and current across self-assembling iron mineral membranes. *Angew. Chem. Int. Ed. Engl.* **54**, 8184-8187 (2015).

44 Moller, F. M., Kriegel, F., Kiess, M., Sojo, V. & Braun, D. Steep pH gradients and directed colloid transport in a microfluidic alkaline hydrothermal pore. *Angew. Chem. Int. Ed. Engl.* **56**, 2340-2344 (2017).

45 Khan, A. I. & O'Hare, D. Intercalation chemistry of layered double hydroxides: recent developments and applications. *J. Mater. Chem.* **12**, 3191-3198 (2002).

46 Estrada, C. F., Sverjensky, D. A. & Hazen, R. M. Selective adsorption of aspartate facilitated by calcium on brucite [$Mg(OH)_2$]. *ACS Earth Space Chem.* **3**, 1-7 (2018).

47 Stein, D., Kruithof, M. & Dekker, C. Surface-charge-governed ion transport in nanofluidic channels. *Phys. Rev. Lett.* **93**, 035901 (2004).

48 Dick, G. J. The microbiomes of deep-sea hydrothermal vents: distributed globally, shaped locally. *Nat. Rev. Microbiol.* **17**, 271-283 (2019).

49 Hsu, H. W. *et al.* Ongoing hydrothermal activities within Enceladus. *Nature* **519**, 207-210 (2015).

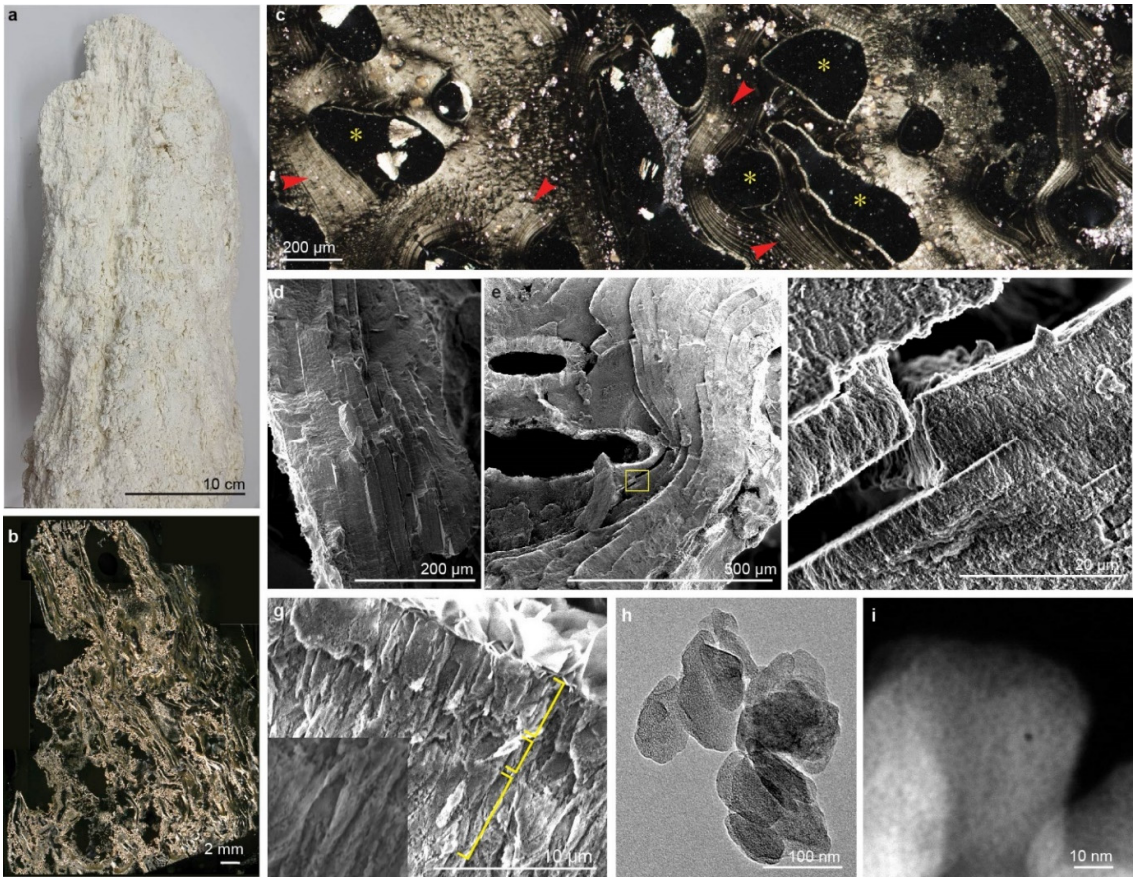

Fig. 1 Structure of hydrothermal vent (HV) precipitates. a, Photograph of HV precipitates collected from the Shinkai Seep Field. **b,c,** Cross-polarized optical microscope images of vertical (**b**) and horizontal slices of HV (cross-section, **c**). In the horizontal slice image, vent fluid channels and periodic line patterns in the HV wall are indicated as yellow asterisks and red arrows, respectively. **d-g,** SEM images of a naturally cleaved HV fragment. **d,e,** Inorganic walls with different cleavage directions. The walls show stratified structures, with the layers following the shape of the wall. **f,** Magnification of the wall (boxed area in **e**) revealing a sublayer structure with consolidated features. **g,** Sublayer structures in different locations of walls. Sublayers 2 to 5-µm thick (yellow square brackets) constituted the wall and exhibited a uniaxial texture. The uniaxial features result from the array of multiple nanoparticles shown in the inset. **h,** TEM image of the crystals constituting the sublayers. **i,** HAADF-STEM image of the crystal with nanopores visible inside.

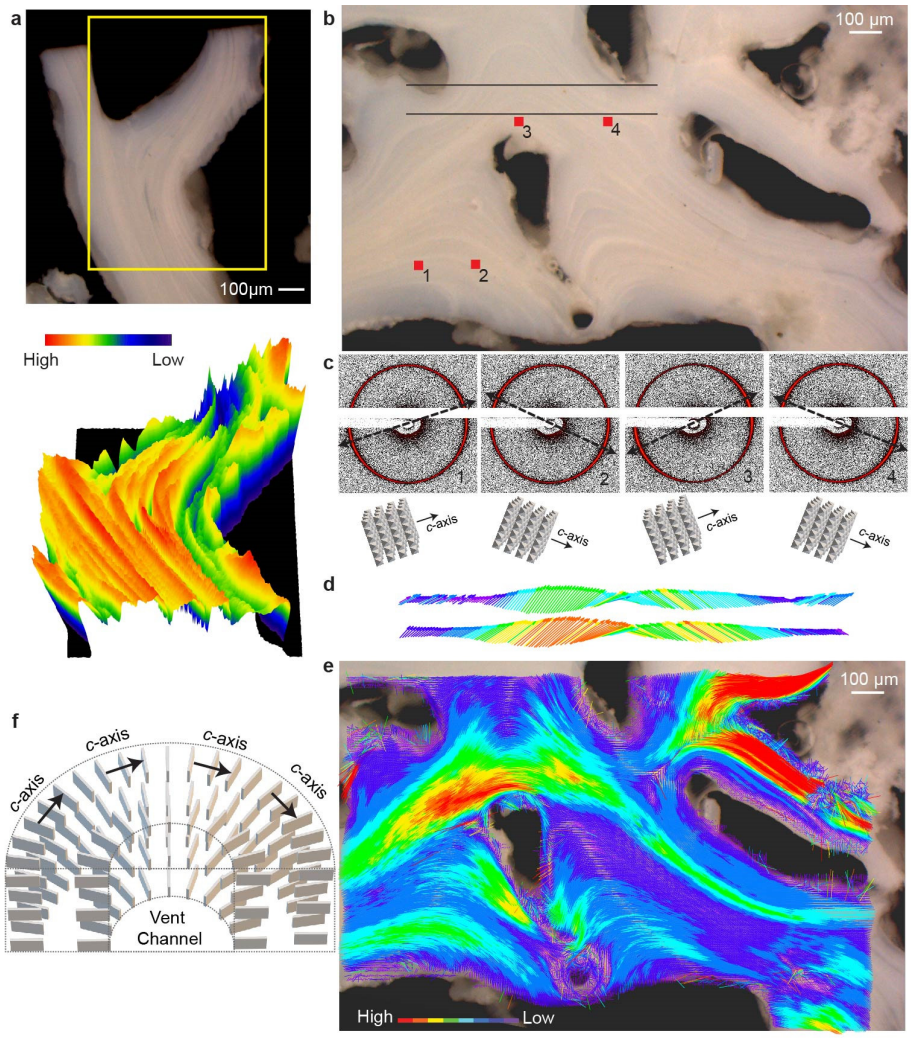

Fig. 2 Synchrotron X-ray diffraction analysis of hydrothermal vent (HV) samples. a, An optical image of a HV slice (above) and its corresponding 3D map of scattering intensity (below). In the 3D intensity map, the scattering intensity at individual scanning points was integrated and converted into single values. **b-e,** WAXS analysis on the HV wall sample. **b,** Optical image of the scanning area. **c,** Selected brucite 001 diffraction patterns at multiple points (red squares in **b**). Black double-headed arrows show the preferred orientation direction of the brucite (001) plane. Schematic images showing the preferred orientation of the brucite layers are shown below the diffraction patterns. The crystal structure of brucite consists of an edge-shared MgO_6 layer in the (001) plane and a layered hydroxide stack along the *c*-axis. **d,** Vector plots showing the direction and intensity of the preferred orientation of the (001) plane. The diffraction patterns at two different locations (line scans) were analyzed and plotted. The black lines in **b** show the location of the line scan. The color and length of the vectors represent the value of the highest scattering intensity of the asymmetric ring. The direction of the vector indicates the orientation of the strongest intensity axis of the asymmetric ring and shows the preferred orientation direction. **e,** 2D map of the vector plot overlayed on the optical image shown in **b**. **f,** Schematic of the brucite (001) plane arrangement around the channel based on the WAXS scanning analysis. The corresponding *c*-axis of brucite is also shown.

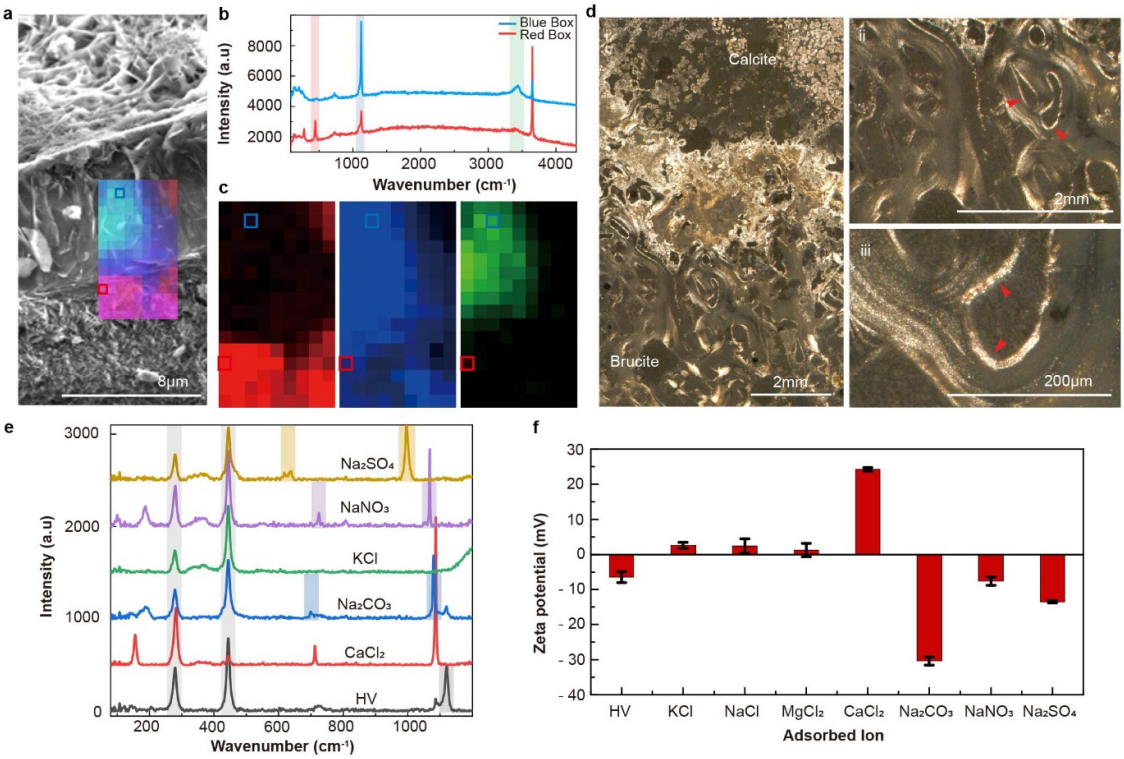

Fig. 3 Ion adsorption in hydrothermal vent (HV) precipitates. a-c, Raman measurement of the HV wall near a fluid channel. **a,** Overlay of the Raman map with the corresponding SEM image. The Raman map is a superimposed image of three specific peaks. The Raman map shows that the brucite and Mg-carbonate crystals are discretely located in the wall, while carbonate ions were present in all regions, indicating the adsorption of carbonate ions by the brucite. **b,** Raman spectra of surface crystals (blue) and HV wall (red) at the positions shown in **a** and **c**. **c,** Map of three specific Raman peaks, red: 442.6 cm^{-1} (brucite lattice vibration, A_{1g}, width 47.5 cm^{-1}), blue: 1109.7 cm^{-1} (carbonate, width 73.4 cm^{-1}), and green: 3420.7 cm^{-1} (interlayered water, width 98.8 cm^{-1}). The corresponding peaks are shown in the spectra in **b**. **d,** A HV slice showing the different crystals inside the HV wall. (i-iii) Consecutive enlargements of the slice. Brucite and calcite crystals are localized at specific areas in the millimeter scale range. From the microscale observation of the HV slice, crystals with different refractive indices covering the surface of several channels were identified (red arrows). **e,f,** Raman spectra (**e**) and zeta potential (**f**) of HV samples after adsorption of various ions. For the analysis, a powdered HV sample was mixed with various ions that are commonly found in sea water: Ca^{2+}, CO_3^{2-}, K^+, NO^{3-}, and SO_4^{2-}. The peaks from the HV sample are indicated in gray and the other Raman peaks attributable to the adsorbed ions are highlighted using the same color of each spectrum. The peaks around 280 and 444 cm^{-1} did not shift in all the spectra, whereas the peaks around 1100 cm^{-1} varied with the type of ion, indicating that ions were exchanged inside the HV wall. The adsorbed ions significantly changed the surface charge of the HV particles. Mean ± s.d. (n = 3).

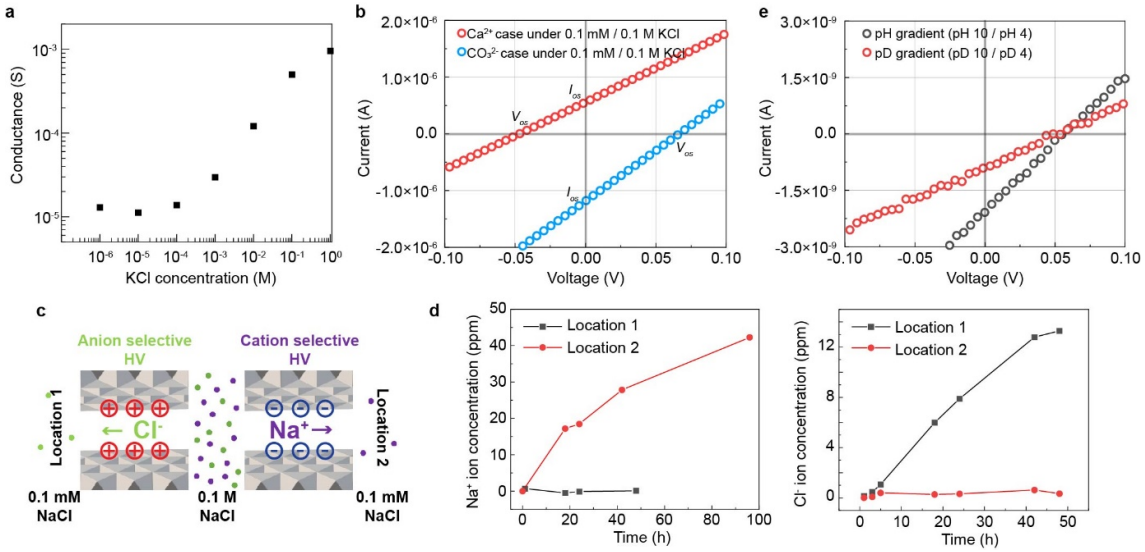

Fig. 4 Ionic transport by hydrothermal vent (HV) precipitates. a, Electrical conductance of HV sample as a function of KCl concentrations with pH 10. **b,** Osmotic energy conversion under a KCl gradient. Current-voltage curves were measured under a 1000-fold salinity gradient (0.1 mM / 0.1 M KCl) for CO_3^{2-}-adsorbed (blue dots) and Ca^{2+}-adsorbed (red dots) HV samples. The redox potential of the electrode was subtracted from measured potential and the diffusion potential (V_{os}) and current (I_{os}) are shown in the figure. The opposite polarity is generated from the different charge selectivity of HV samples. **c,** Schematic illustration of the experimental setup for the ion selectivity measurements. The anion- and cation-selective HV samples were placed between reservoirs, and the HVs were exposed to alternating NaCl concentrations (0.1 mM / 0.1 M / 0.1 mM). **d,** Concentration changes of Na^+ and Cl^- ions over time at locations 1 and 2 were measured and plotted. **e,** Osmotic power generation in the presence of pH (pH 10/ pH 4) and pD (pD 10/ pD 4) gradients. The cation-selective (CO_3^{2-}-adsorbed) HV sample was used for the analysis.

Acknowledgement

The authors would thank the *Shinkai 6500* operation team and the crew of the R/V *Yokosuka* for their professional support for sampling of HV precipitates during the YK14-13 cruise. The HV sample was collected using the Shinkai 6500 manipulators during dive #1404 on cruise YK14-13 in 2014 (ID; 12541-14001_6K1404-R05). This study was conducted under the special use permit of US Fish and Wildlife Service for studies in the Mariana Trench Marine National Monument (#12541-14001). The synchrotron radiation experiments were performed at RIKEN Targeted Proteins Beamline (BL32XU) and RIKEN Structural Biology I (BL38B1) in SPring-8 with the approval of RIKEN (Proposal No. 20210086). This work was supported by RIKEN Special Postdoctoral Researchers (SPDR) fellowship to H.-E. L. and by JSPS Grant-in-Aid for Scientific Research to R. N. (22H05153) and T. O. (15H05468 and 19K14830). We thank Daishi Inoue for technical support and discussion on WAXS sample preparation.

Author contributions

H.-E. L., S. E. M. and R. N. conceived the idea and designed the experiments. T. O. and Y. O. collected hydrothermal vent precipitates. T. O. and Masahiro Y. prepared specimens. H.-E. L. performed the experiments and characterization. H. O. and H.-E. L. processed the diffraction peaks and generated 2D plots. K. A., T. H., K. H., Y. K., H. M., and Masaki Y. carried out the X-ray experiments. D. H., K. A., and H.-E. L. analyzed the X-ray diffraction results. A. Y. conducted nitrogen adsorption/desorption analysis. H.-E. L. conducted electrical property measurements with contributions from R. N., A. Y., H. O., J.-E. L., and K. T. N. H.-E. L. and R. N. wrote the paper with contributions from S. E. M. and H. O., and feedback from all authors. All authors discussed the results and commented on the manuscript.